Lecture 6 — Defects in Crystals.

1 Introduction

In the first five lectures, we have focussed our attentions on the methodologies used to describe crystal symmetry and on the scattering techniques employed to study the arrangement of atoms and spins in crystals (electronic, nuclear and spin densities). Throughout this discussion, we have explicitly assumed that the crystalline order is "perfect" — in other words, that translational symmetry is strictly valid. The only allowance we made for deviations from one unit cell to the next is through the introduction of the Debye-Waller factors, the effect of which, as we have seen, is to "spread out" the scattering densities in a fashion similar to the atomic scattering factors. In this lecture, we will explicitly consider crystal "imperfections" of different kinds, starting from the simplest form of translational symmetry breaking (the effects arising from the finite size of the crystals) and considering in turn other, more complex types of defects: "point" defects, correlated defects and "line" or "plane" defects (dislocations or stacking faults). As we shall see, all these defects give rise to particular kinds of scattering, most often away from the Bragg peaks. We will also introduce a new experimental technique — transmission electron microscopy — and describe its relevance in the study of crystal defects.

1.1 Space and time scales: coherence

When dealing with crystal imperfections, one of the first questions one should ask is whether they will contribute *coherently* (i.e., amplitudes are summed) or *incoherently* (i.e., intensities are summed) to the diffraction patterns.

Let us make this clear with a simple example: consider an inhomogeneous alloy, in which the composition and the lattice constants varies on the scale of millimetres. Clearly, the different regions of the crystal will scatter independently, each region being in essence a "perfect crystal". The result, therefore, with be the *incoherent* superposition of different patterns. In this example, each hkl will produce a set of independent Bragg peaks (corresponding to the different lattice constants), which will typically appear as a *broadening* of the scattered reflections. Let us now imagine to "shrink" the lengthscale of the composition and lattice parameters fluctuations down to nanometre sizes. Here, the different compositions will scatter *coherently*, and the appropriate picture is that of an *average lattice*. In the different regions, the atoms will be displaced away from the average positions, and this, as we know by now, will produce a *reduction* of the Bragg intensity at high $\mathbf{q}$, in complete analogy to the Debye-Waller factors. Furthermore, the displacements will be *correlated* (i.e., nearby atoms will tend to be displaced in the same direction). Later

in this lecture, we will learn that this produces *diffuse scattering* away from the Bragg peaks. At different lengthscales, he diffraction patterns will be therefore **qualitatively different**. At what point, between millimetres and nanometres, does this qualitative transition occur? We can intuit that the lengthscale where the transition occurs might be set by the *probe*, i.e., that there mat be intrinsic **coherence lengths** for X-rays, neutrons, electrons etc. A very similar argument may be construed for *timescales*. If the positions of the atoms in the crystal "fluctuate", e.g., due to phonons, do the different configurations occurring at different times contribute coherently or incoherently to the diffraction pattern? If the timescale of the fluctuations if of the order of seconds, the latter will be true, but, as the timescale of the fluctuations is reduced, this will no longer be the case. What is the typical **coherence time** of the different probes?

A complete treatment of the correlation lengths and times is to complex to be presented here, but the following points should provide a good idea of the issues involved.

- One distinguishes between **transverse** and **longitudinal** coherence lengths, perpendicular and parallel, respectively, to the direction of the beam.

- For a quasi-parallel beam geometry (as it is typical of a diffraction instrument), the **transverse coherence length** ξ_t is proportional to the wavelength and inversely proportional to the beam divergence α ($\xi_t = \lambda/\alpha$). Here, the beam divergence is defined as *the angle subtended by the source as seen from the sample*. The derivation is analogous to that of the double-slit experiment, and corresponds to the distance between slits where the interference pattern is lost. For for typical diffraction instruments, the beam divergence varies between a few mrad (lab diffractometers) down to a tenth of mrad (synchrotrons), so for $\lambda = 1\mathring{A}$, ξ_t varies between a few tens of nm up to about 1 μm. Highly coherent X-ray beams (several tens of μm) are employed for special studies (lensless imaging, "speckle" patterns), revealing the shape and internal structure of large crystal domains. Neutron beams have comparatively relaxed divergences, and typical coherence lengths are 1000-2000 Å.

- For geometries employing focussing, (e.g., electron diffraction) it is possible to manipulate the coherence domain by varying the focal plane where the diffraction pattern is formed (see below). If the *diffraction pattern* is in focus, the coherence length is essentially limited by the aberration of the lenses, and can be as large as for X-rays, in spite of the fact that the wavelength employed are 1-2 orders of magnitude smaller. If the *sample* is in focus, the transverse coherence length is much smaller (down to atomic sizes), so that each detector pixel receives a coherent contribution of a **column** of atoms in the direction of the beam. In this case, the coherence domain coincides with the **resolving power** of the instrument (see below).

- The **longitudinal coherence length** is inversely proportional to the relative wavelength spread of the beam: $\xi_l = \frac{1}{2}\lambda/(\Delta\lambda/\lambda)$. High-resolution monochromators at synchrotron sources typically yield $\Delta\lambda/\lambda \sim 0.5 - 1 \times 10^{-4}$, so at 1 Å ξ_l is about 1 μm. The wavelength spread of neutron and electron beams is typically 10 times and 100 times larger, respectively.

- The **coherence time** can be calculated using the uncertainty principle as $\tau = \hbar/\Delta E$ or from the relation $\tau = \xi_l/v$, yielding the same result apart for a factor of the order 1. Adopting the first approach, we obtain

$$\begin{aligned} \tau &= \frac{1}{\pi^2}\frac{m\lambda^2}{\hbar}\left(\frac{\Delta\lambda}{\lambda}\right)^{-1} \text{for particles with mass} \\ \tau &= \frac{1}{2\pi}\frac{\lambda}{c}\left(\frac{\Delta\lambda}{\lambda}\right)^{-1} \text{for photons} \end{aligned} \tag{1}$$

  The prefactor is 1.6×10^{-14} [secÅ^{-2}] for neutrons, 0.9×10^{-17} [secÅ^{-2}] for electrons and 5×10^{-20} [secÅ^{-1}] for photons. Using the wavelengths and monochromaticity values mentioned above, we find that coherence times for neutrons, photons and 100 Kev electrons are in the picosecond, femtosecond and tens of attosecond ranges, respectively.

2 Finite size effects

Up to this point, we have consider the crystal lattice to be of infinite extent. As we have seen, the cross section becomes then a series of delta functions, centered on the RL nodes. We can relax our approximation by starting form eq. 6 in Lecture 5 (the cross section) and solve explicitly for the finite summations. in fact, we need not make any particular approximation other than the fact that the crystal should be composed of N_1,N_2 and N_3 unit cell in the $\mathbf{a}_1$, $\mathbf{a}_2$ and $\mathbf{a}_3$ directions, respectively. Remembering that

$$\sum_{n=-N}^{N} e^{-inx} = \frac{\sin\left((2N+1)\frac{x}{2}\right)}{\sin\frac{x}{2}} \tag{2}$$

after some straightforward math (in each direction, $x = \mathbf{q}\cdot\ \mathbf{a}_i$) we obtain

$$\boxed{\frac{d\sigma}{d\Omega} = \left[\prod_i \frac{\sin^2\left(N_i\frac{1}{2}\mathbf{q}\cdot\ \mathbf{a}_i\right)}{\sin^2(\frac{1}{2}\mathbf{q}\cdot\ \mathbf{a}_i)}\right]|F(\mathbf{q})|^2\left[\boldsymbol{\varepsilon}\cdot\boldsymbol{\varepsilon}'\right]^2} \tag{3}$$

The diffraction pattern from a small single crystal taken with *coherent* radiation, i.e., radiation with *coherence length* (=wavepacket length/width) larger than the crystal, will display **3-dimensional fringes**, as typical of the function $\sin^2(Nx)/\sin^2 x$. However, for typical experiments with incoherent radiation, the number of unit cells is set by the coherence length of each photon rather than by the crystal size, and the oscillations will be smeared out. In this case, we can replace the oscillatory functions with a *Gaussian* function with the same maximum and same area:

$$\frac{\sin^2 Nx}{\sin^2 x} \rightarrow N^2 e^{-(Nx)^2/\pi} \tag{4}$$

Observing that $\prod_i N_i = N_c$, the total number of unit cell in the crystal, we obtain

$$\boxed{\frac{d\sigma}{d\Omega} = N_c^2 \left[\prod_i e^{-(N_i \frac{1}{2}\mathbf{q}\cdot\,\mathbf{a}_i)^2/\pi}\right] |F(\mathbf{q})|^2 \left[\boldsymbol{\varepsilon}\cdot\boldsymbol{\varepsilon}'\right]^2} \tag{5}$$

where the Gaussian functions have variance and FWHM

$$\begin{aligned} \sigma_i^2 &= \frac{2\pi}{N_i^2 a_i^2} \\ FWHM &= \frac{4\sqrt{\pi \ln 2}}{N_i a_i} \end{aligned} \tag{6}$$

We can therefore conclude that:

- The **cross section at a given q** is proportional to N_c^2.
- The **width** in **q** is *inversely proportional to the number of unit cells along that direction*.
- The **integrated cross section** in three dimensions (remember the Gaussian integral $\sqrt{2\pi\sigma^2}$) is therefore proportional to N_c, which reproduces the result we obtained for the infinite crystal (eq. 8, lecture 5).

3 Beyond the perfect-crystal approximation: diffuse scattering

Finite-size effects only generate scattering in the vicinity of the "ideal" Bragg positions, leaving the integrated intensity of the reflection unaltered. In this section, we will demonstrate that

additional scattering is generated whenever either the atomic scattering factors or the positions of individual atoms deviate from the average values and/or the "ideal" lattice sites. In general, this additional scattering is present throughout reciprocal space, and is therefore known as **diffuse scattering**. In the remainder of this section, we will consider the deviations from perfect periodicity as **static**. In other words, we will imagine that the scattering process occurs coherently from a **frozen snapshot** of the crystal. To estimate the full scattered intensity, at the end, we will undertake a time/thermal averaging process on the scattered intensities. This is a very good approximation in the case of X-rays (and electrons), since the coherence times are *much shorter than phonon frequencies*. For neutrons, where this is clearly not the case, a more complex treatment is required, but qualitatively similar considerations (with some caveats) can be applied.

3.1 Classification of disorder in crystals

We will here consider two types of disorder:

- **Substitutional disorder** is typical of alloys and, more generally, of solid solutions. It occurs when more that one atonic species can reside on the same crystallographic site, and gives rise to a fluctuation of the atomic scattering factor around an "average" value, the latter reflecting the average composition of the alloy. For example, in a 67%Cu-33%Au "random" alloy, Cu and Au occupy the same crystallographic sites of the FCC structure. To calculate the Bragg scattering from such an alloy, one should use the *average* atomic scattering factor ($f_{ave}(0) = 45.7$). However, *locally*, the scattering factor varies between that of Cu ($f_{Cu}(0) = 29$) and Au ($f_{Au}(0) = 79$). This local fluctuation, as we shall see, gives rise to diffuse scattering. Substitutional disorder is almost always **static**, since atoms in alloys do not usually move from one site to the next, but counter-examples do exist (e.g., in the case of fast ion conductors).
- *Dynamic* **displacive disorder** is present in all materials even at zero temperatures, due to phonons and zero-point motion. In addition to scattering contrast fluctuations, substitutional disorder can itself produce *static* displacive disorder, since different species have in general different atomic radii.

3.2 Simple diffuse scattering calculations

We shall now calculate the *full* scattering cross section for an (infinite) crystal in the presence of both substitutional and displacive disorder. To simplify the formalism, we will perform this calculation in the case of a crystal with one atom per unit cell, but the extension to more complex

structures is completely straightforward. Let us therefore re-write the cross section in eq. 6, Lecture 5 in this case.

$$\frac{d\sigma}{d\Omega} = r_0^2 \mathcal{P}(\gamma) \left(\sum_j \sum_i e^{-i\mathbf{q}\cdot(\mathbf{r}_i - \mathbf{r}_j)} \right) f_i(\mathbf{q}) f_j^*(\mathbf{q}) \tag{7}$$

In eq. 7, $\mathbf{r}_i$ represent the *actual* positions of the atoms, while we indicate with $\mathbf{R}_i$ the position of the lattice nodes. Moreover, we will write

$$\mathbf{r}_i = \mathbf{R}_i + \mathbf{u}_i \tag{8}$$

where the $\mathbf{u}_i$ are the *displacements* away from the lattice nodes and are "small" (see below). With the additional notation $\mathbf{R}_{ij} = \mathbf{R}_i - \mathbf{R}_j$ and $\mathbf{u}_{ij} = \mathbf{u}_i - \mathbf{u}_j$ we can write:

$$\frac{d\sigma}{d\Omega} = r_0^2 \mathcal{P}(\gamma) \sum_{\mathbf{R}_{ij}} e^{-i\mathbf{q}\cdot\mathbf{R}_{ij}} \sum_{Pairs\, with\, \mathbf{R}_{ij}} \left[f_i(\mathbf{q}) f_j^*(\mathbf{q}) e^{-i\mathbf{q}\cdot\mathbf{u}_{ij}} \right] \tag{9}$$

In eq. 9, we have rearranged the double summation, so that the rightmost sum runs over all pairs of unit cells joined by a given vector $\mathbf{R}_{ij}$, whereas the leftmost sum runs over these vectors. Using, for example, periodic boundary conditions, we find that for each $\mathbf{R}_{ij}$, there are exactly N pairs of sites joined by it (N being the total number of atoms in the crystal. We can therefore re-write eq. 9 as:

$$\frac{d\sigma}{d\Omega} = N r_0^2 \mathcal{P}(\gamma) \sum_{\mathbf{R}_{ij}} e^{-i\mathbf{q}\cdot\mathbf{R}_{ij}} \left\langle f_i(\mathbf{q}) f_j^*(\mathbf{q}) e^{-i\mathbf{q}\cdot\mathbf{u}_{ij}} \right\rangle_{\mathbf{R}_{ij}} \tag{10}$$

We can subtract from eq. 10 the Bragg scattering cross section to obtain the expression for the non-Bragg or **diffuse scattering** (we stress, once again, that the *average* atomic scattering factor is used to calculate the Bragg scattering):

$$\left(\frac{d\sigma}{d\Omega} \right)_{diff} = N r_0^2 \mathcal{P}(\gamma) \sum_{\mathbf{R}_{ij}} e^{-i\mathbf{q}\cdot\mathbf{R}_{ij}} \left\langle f_i(\mathbf{q}) f_j^*(\mathbf{q}) e^{-i\mathbf{q}\cdot\mathbf{u}_{ij}} - |f_{ave}(\mathbf{q})|^2 e^{-2W} \right\rangle_{\mathbf{R}_{ij}} \tag{11}$$

where the sign $\langle\rangle_{\mathbf{R}_{ij}}$ indicates the *average* of the quantity within it over all the pairs in the coherence domain joint by the vector $\mathbf{R}_{ij}$.

3.2.1 Diffuse scattering from uncorrelated substitutional disorder

Here, we will make the slightly unrealistic assumption that the atoms are not displaced at all from their ideal lattice sites, and consider the diffuse scattering arising from purely substitutional disorder ($\mathbf{u}_{ij} = 0$). We can write

$$\left(\frac{d\sigma}{d\Omega}\right)_{diff} = Nr_0^2\mathcal{P}(\gamma)\sum_{\mathbf{R}_{ij}} e^{-i\mathbf{q}\cdot\mathbf{R}_{ij}}\left\langle f_i(\mathbf{q})f_j^*(\mathbf{q}) - |f_{ave}(\mathbf{q})|^2\right\rangle_{\mathbf{R}_{ij}} \tag{12}$$

If the sites have random occupancy, for $i \neq j$ the average is identically zero for all $\mathbf{R}_{ij}$, so only the autocorrelation term $i = j$ survives, yielding

$$\boxed{\left(\frac{d\sigma}{d\Omega}\right)_{diff} = Nr_0^2\mathcal{P}(\gamma)\left[(|f(\mathbf{q})|^2)_{ave} - |f_{ave}(\mathbf{q})|^2\right]} \tag{13}$$

For example, for a binary alloy with species A and B and concentrations C_A and $1 - C_A$, we obtain

$$\left(\frac{d\sigma}{d\Omega}\right)_{diff} = Nr_0^2\mathcal{P}(\gamma)C_A(1 - C_A)|f_A(\mathbf{q}) - f_B(\mathbf{q})|^2 \tag{14}$$

As we can see, these cross sections are slowly varying in q, since they are only modulated by the atomic scattering factors, and have their maximum near $q = 0$.

3.2.2 Diffuse scattering from uncorrelated displacements

Let us now assume that we have a single atomic species ($f_i = f_j = f_{ave}$) and that the displacements of atoms i and j are not correlated with each other. If $i \neq j$,

$$\left\langle e^{-i\mathbf{q}\cdot\mathbf{u}_{ij}}\right\rangle = \left\langle e^{-i\mathbf{q}\cdot\mathbf{u}_i}\right\rangle\left\langle e^{-i\mathbf{q}\cdot\mathbf{u}_j}\right\rangle = e^{-2W} \tag{15}$$

so $\mathbf{R}_{ij}$ vectors joining different atoms do not give any contributions to the diffuse scattering. The only surviving term is the autocorrelation term, for which $\mathbf{u}_{ij} = 0$. Therefore,

$$\boxed{\left(\frac{d\sigma}{d\Omega}\right)_{diff} = Nr_0^2\mathcal{P}(\gamma)|f(\mathbf{q})|^2\left(1 - e^{-2W}\right)} \tag{16}$$

As we can see from eq. 16, the diffuse scattering from uncorrelated displacements is a slowly varying function of $\mathbf{q}$; it is zero near the origin of the reciprocal space and *increases* with q (it is in the first approximation proportional to q^2), only to decay again with the decay of the atomic scattering factors.

3.3 General treatment of displacive disorder and thermal diffuse scattering

In the two simple examples we proposed above, we have treated the deviations from the average structure as completely uncorrelated from site to site. The result, in both cases, is a form of diffuse scattering that has very little structure in reciprocal space. In the extreme case of *neutron* studies of substitutional disorder, the atomic form factor is a constant, and the resulting diffuse scattering is completely flat.

In realistic cases, correlations are almost always present: even in disordered alloys, a given species may have a "preference" to be surrounded by atoms of the same kind or, quite frequently, of a different kind, so near-neighbour probabilities are generally different from the average. These correlations are lost after a few unit cells, and they are referred to as **short-range order**. In this case, beside the autocorrelation term, additional terms in the summation (eq. 12) will be non-zero, giving rise to a more structured diffuse scattering pattern. Note that each $\mathbf{R}_{ij}$ pair that corresponds to a definite correlation will contribute with a Fourier component $exp(\mathbf{R} \cdot \mathbf{R}_{ij})$ (or $\cos \mathbf{R} \cdot \mathbf{R}_{ij}$ in the centrosymmetric case) to the diffuse scattering.

The **correlated displacements** due to thermal vibrations are of even longer range: an ideal plane-wave phonon involves all sites of the crystal, and therefore involves all terms in the summation (eq. 11). The correlation terms $\mathbf{u}_{ij}$ will typically involve sums and differences of sines and cosines, and since they appear in the exponential, the summation over an infinite number of pairs cannot be performed analytically. The typical approach is to expand the exponential in Taylor series. This is done as follows: for simplicity, let us rewrite eq. 11 in the case of pure displacive disorder (no substitutional disorder):

$$\left(\frac{d\sigma}{d\Omega}\right)_{diff} = N r_0^2 \mathcal{P}(\gamma) \sum_{\mathbf{R}_{ij}} e^{-i\mathbf{q}\cdot\mathbf{R}_{ij}} |f(\mathbf{q})|^2 \left[\left\langle e^{-i\mathbf{q}\cdot\mathbf{u}_{ij}}\right\rangle_{\mathbf{R}_{ij}} - e^{-2W}\right] \tag{17}$$

Next, we will use again eq. 13, Lecture 5, which is valid for small displacements or harmonic displacements:

$$\left\langle e^{-i\mathbf{q}\cdot\mathbf{u}_{ij}}\right\rangle = e^{-\frac{1}{2}\left\langle[\mathbf{q}\cdot\mathbf{u}_{ij}]^2\right\rangle} \tag{18}$$

Finally, we expand the exponential in eq. 18 in Taylor series:

$$\begin{aligned}\left(\frac{d\sigma}{d\Omega}\right)_{diff} &= Nr_0^2\mathcal{P}(\gamma)\sum_{\mathbf{R}_{ij}} e^{-i\mathbf{q}\cdot\mathbf{R}_{ij}}|f(\mathbf{q})|^2\left\{\left[-\frac{1}{2}\left\langle[\mathbf{q}\cdot\mathbf{u}_{ij}]^2\right\rangle + 2W\right]\right. \\ &\quad \left.+\left[\frac{1}{8}\left\langle[\mathbf{q}\cdot\mathbf{u}_{ij}]^2\right\rangle^2 - 2W^2\right] + \ldots\right\} \\ &= I_1 + I_2 + \ldots \end{aligned} \tag{19}$$

The different terms in eq. 19 are known as first-order, second-order etc., diffuse scattering.

3.3.1 First-order thermal diffuse scattering

In well-ordered crystals, the most important contribution to the diffuse scattering is that from the displacement patterns due to phonons. This type of diffuse scattering is known as Thermal Diffuse Scattering or TDS. The first-order term in eq. 19 is often the dominant contribution, particularly at moderate temperatures. The calculation of diffuse scattering for monoatomic solid is not inaccessible at the present level, but it is rather lengthy. Here, we summarise the main steps and present the final result, so that its structure can be analysed.

- Only phonons with the same wavevector $\mathbf{k}$ and the same branch index contribute coherently to first-order TDS. The scattering from one such phonon is not difficult to calculate: it generate *satellite peaks* at $\pm\mathbf{k}$ around any given Bragg peaks.
- One needs to sum the *scattered intensity* of phonons with different wavevectors, taking into account the fact that their amplitude is related to the thermal population.
- The final result is:

$$\boxed{\left(\frac{d\sigma}{d\Omega}\right)_{1^{st}TDS} = Nr_0^2\mathcal{P}(\gamma)\frac{\hbar}{2M}\sum_j \frac{1}{\omega_j(\mathbf{q})}\coth\left(\frac{\hbar\omega_j(\mathbf{q})}{2k_BT}\right)|F_j(\mathbf{q})|^2} \tag{20}$$

  where the sum is over the different phonon branches and

$$F_j(\mathbf{q}) = f(\mathbf{q})e^{-W}\left[\mathbf{q}\cdot\mathbf{e}_j(\mathbf{q})\right] \tag{21}$$

  is the so-called **one-phonon structure factor** and $\mathbf{e}_j(\mathbf{q})$ is the polarisation vector of phonon branch j at the wavevector $\mathbf{q}$. In order to evaluate the quantities $\mathbf{e}_j(\mathbf{q})$ and $\omega_j(\mathbf{q})$, one needs to reduce $\mathbf{q}$ to the first Brillouin zone in the usual way.

- The function $\frac{1}{\omega_j(\mathbf{q})} \coth\left(\frac{\hbar\omega_j(\mathbf{q})}{2k_BT}\right)$ **decreases rapidly** with increasing frequency. Therefore **low-energy, acoustic phonons provide the largest contribution to first-order TDS**. For the same reason, the TDS diverges at the Bragg peak positions and is minimum between the Bragg peaks.

- When the same reduced wavevector is considered in different Brillouin zones, one finds that the cross section is proportional to q^2, similar to the diffuse scattering due to uncorrelated displacements (eq. 21).

4 Scattering from non-crystalline solids and liquids

Our discussion of the scattering cross sections for "defective" crystal would not be complete without a mention of the most extreme form of defects — the complete loss of crystalline order, as in the case of non-crystalline solids (glasses) or liquids. In this case, it is no longer possible to define a crystal lattice; nevertheless, the formalism to calculate the scattering cross section is very similar to the one we have already encountered (eq. 9). The main difference is that, for obvious reasons, decomposing position vectors in $\mathbf{R}_{ij}$ and $\mathbf{u}_{ij}$ will no longer make sense, and we will therefore employ the original notation $\mathbf{r}_{ij}$

$$\frac{d\sigma}{d\Omega} = r_0^2 \mathcal{P}(\gamma) \sum_{m=1}^{N} \sum_{\mathbf{r}_{ij}} f_i(\mathbf{q}) f_j^*(\mathbf{q}) e^{-i\mathbf{q}\cdot\mathbf{r}_{ij}} \tag{22}$$

where the first sum runs over all the atoms in the sample. For simplicity, we will proceed from here assuming that all the atoms in the sample are the same, as appropriate, for example, for a monoatomic liquid like mercury. The extension to polyatomic liquids or glasses is rather straightforward but requires a heavier notation. With our assumption, we can extract $N|f(\mathbf{q})|^2$ from all the summations and replace the sums with averages; we will also isolate the autocorrelation term ($\mathbf{r}_{ij} = 0$) which yields 1:

$$\frac{d\sigma}{d\Omega} = N r_0^2 \mathcal{P}(\gamma) |f(\mathbf{q})|^2 \left[1 + \sum_{\mathbf{r}_{ij} \neq 0} \langle e^{-i\mathbf{q}\cdot\mathbf{r}_{ij}} \rangle \right] \tag{23}$$

We now want to take advantage of the fact that, in a disordered sample, if a vector $\mathbf{r}_{ij}$ connecting two atoms is present, then all other vectors with the same modulus r_{ij} will also be present with equal probability somewhere in the sample. This will enable us average over the angular variables and replace the summation in eq. 23 with a sum over r_{ij}. In doing so, we have to account for the

fact that any given atom may be surrounded by more than one atom at the same distance r_{ij}, and we will do so by introducing the **average coordination number** $n(r_{ij})$.

$$\frac{d\sigma}{d\Omega} = Nr_0^2\mathcal{P}(\gamma)|f(\mathbf{q})|^2 \left[1 + \sum_{r_{ij}\neq 0} n(r_{ij}) \frac{1}{4\pi} \int_0^\pi e^{-iqr_{ij}\cos\theta} \sin\theta d\theta d\phi\right] \tag{24}$$

The integral is straightforward and yields $4\pi \sin qr_{ij}/qr_{ij}$.

$$\boxed{\frac{d\sigma}{d\Omega} = Nr_0^2\mathcal{P}(\gamma)|f(\mathbf{q})|^2 \left[1 + \sum_{r_{ij}\neq 0} n(r_{ij}) \frac{\sin qr_{ij}}{qr_{ij}}\right]} \tag{25}$$

The structure of eq. 25 clearly illustrates the main feature of the scattering form non-crystalline materials: the cross section only depends on q, so the scattering will occur as **uniform spheres in reciprocal space**. Analysis of the scattering will provide information about the **average coordination number** at every distance r_{ij} around a given atom. More details about this, with particular reference to the Pair Distribution Function analysis method, are provided in Appendix I (see also [2]).

5 Other defects in crystals: point defects, dislocations and planar defects

In this section, we will be concerned with a few additional modes of departures from perfect crystal ordering, known as **point defects**, **dislocations** and **planar defects**. These defects are associated with points, lines or planes in the crystal, and move slowly or not at all, so they can generally be considered as static, as far as diffraction is concerned.

5.1 Point defects

A point defect occurs when the crystal periodicity is primarily broken at one lattice site or at a few adjacent sites, although its influence can propagate far away into the crystal (see below). The simplest examples of a point defect are **substitutions vacancies** and **interstitials**, in which, respectively, atoms on a given site are replaced by a different species, are absent altogether or occupy a position that is usually unoccupied. **Substitutional disorder in alloys** can be thought as an extreme example of a high density of point defects. Point defects often occurs in pairs up to

maintain stoichiometry or charge neutrality, as in the case of Frenkel defects (a vacancy and an interstitial) or Schottky defects (vacancy of ions with opposite charge). In the case of **extended defects**, the coordination environment around the defect site is modified to approximate the preferred environment of the new species. For example, if a cation with a preference for tetrahedral coordination is substituted on an octahedral site, the six surrounding anions can be distorted and one or two can be missing altogether, forming an extended defect.

If present in sufficient concentration, point defects can give rise to diffuse scattering, in complete analogy to substitutional disorder. Another form of diffuse scattering associated with point defects is **Huang scattering**: this arises from the static displacement field due to the elastic deformation of the lattice around the defect, and its treatment is analogous to that of first-order TDS.

5.2 Dislocations

Dislocations are linear defects that commonly form in metals as a result of the application of stresses, e.g, due to repeated bending. They play an important role in both the strength and the failure of materials: **work hardening** (such as beating a red-hot piece of metal on an anvil) has been used for centuries by blacksmiths to introduce dislocations into materials, increasing their yield strengths. On the other hand, the infamous **metal fatigue fracture** (responsible, for example, for the De Havilland Comet disasters) are initiated by dislocations, which eventually form persistent slip bands that nucleate short cracks

Two main types of dislocations are identified: **edge dislocations** and **screw dislocation**, although most real dislocation are intermediate between these types. They are characterised by two direction vectors: the **dislocation direction** — the direction of the linear structure in question, and the **Burgers vector** — the principal direction of the strain (displacement) field near the dislocation.

5.2.1 Burgers vectors for edge and screw dislocations

The classic definition of the Burgers vector is the following (see fig. 1 and 2): Let us consider a part of the crystal that is *free* from any defect, and let us define a closed loop of atoms. Let us now insert the dislocation so that the dislocation line is *inside* and *perpendicular to* the loop. The strain (displacement) field generated by the defect will displace the existing atoms, so that the rectangle will be deformed, whilst, by definition, remaining a closed loop. If the rectangle is deformed into a trapezium, the Burgers vector will be *perpendicular* to the dislocation line (**edge dislocation**, fig. 1). If the rectangle is deformed into a 3-dimensional shape, the Burgers vector will be *parallel* to the dislocation line (**screw dislocation**, fig. 2).

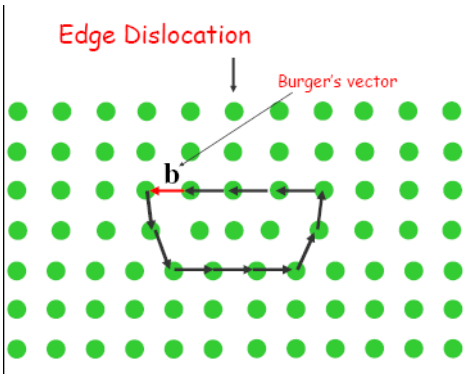

Figure 1: An edge dislocation and its associated Burgers vector. An edge dislocation arises when a plane of atoms is abruptly terminated within the crystal. The displacement field around the edge dislocation is defined by its Burgers vector, and, is **perpendicular to the dislocation line**.

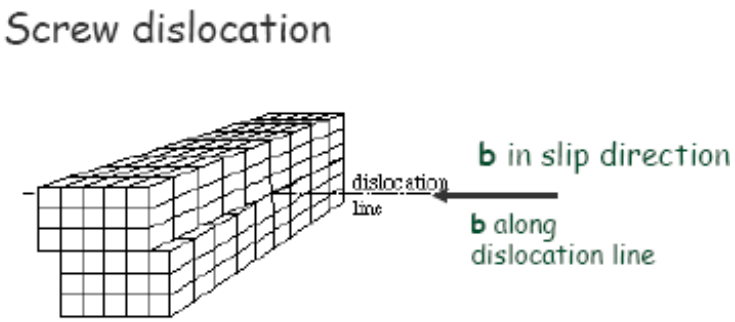

Figure 2: A screw dislocation and its associated Burgers vector. We can imagine that a screw dislocation is generated by "slicing" a plane through the crystal up to a certain line, and by displacing the atoms on one side of the plane by one unit cell along the direction of the line. The displacement field around the edge dislocation is defined by its Burgers vector, and is **perpendicular to the dislocation line**.

5.3 Stacking faults

The last family of crystal defects we will consider in this lecture are the *planar defects*. As the word implies, the defect originated at a planar locus in the crystal, although the strain field can propagate some way away from the plane. Although other types of planar defects exist (for example, the **twin planes**), here we will only consider the **stacking faults**.

Staking faults are defects in the "stacking" of atomic layers — most commonly a fault in the stacking sequence of the layers, a missing layer or an added layer, either of the same type or of a different type with respect to the bulk layers. Unsurprisingly, **stacking faults are common**

in layered structures, but are also encountered in isotropic structures: in fact, perhaps the best known type of stacking fault occurs in FCC metals, and is a fault of the ...ABCABCABC... stacking sequence of the (111) layers, as, for example, in ...ABCABABCABC... Stacking faults of this type can be described as a **displacement (slip)** of an entire plane of atoms **perpendicular** to the fault plane, so that the fault is described by two vectors: the **stacking vector** (perpendicular to the fault plane) and the **slip vector**, describing the displacement direction of the plane of atoms. The slip vector plays a similar role to the Burgers vectors in the imaging of stacking faults by TEM (see below). In this case of the (111) faults in FCC metals, the **slip vector** is along the $(\bar{2}11)$ direction or its equivalents (fig. 3).

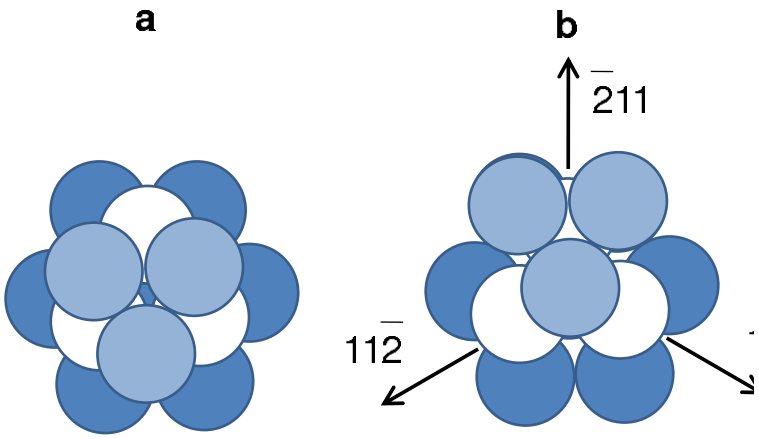

Figure 3: **A**: a portion of the unfaulted FCC structure, with stacking sequence ...ABCABCABC....**B** A stacking fault, in which the "A" layer is inserted instead of a "C", and the corresponding possible slip vectors.

6 Experimental techniques: Electron Microscopy

6.1 Rationale and brief history of electron microscopy

In the absence of aberrations, the resolving power of a microscope is given by the well-known formula $R = \kappa\lambda/n\sin\alpha$, where $n_0 \sin\alpha$ is the **numerical aperture**, n_0 is the refractive index in object space and α is the semi-angle subtended by the object at the lens (or stop). The constant κ depends on the coherence length of the light, but the typical value of 0.61 is generally adopted.

For visible light (e.g. 550 nm), the largest achievable numerical apertures is about 1.6, yielding a " diffraction limited" resolution of about 200 nm. X-ray beams have much shorter wavelengths, but X-ray lenses are complex, high-precision objects and are limited to very small numerical apertures. With wavelengths of a few hundredths of Å (Table 1) and the possibility of achieving numerical apertures comparable to those of optical microscopy, a microscope based on an electron beam should be able to resolve feature well below the inter-atomic spacing. In practice, the resolution of an electron microscope is limited by optical aberrations rather than diffraction, but resolutions below 1 Å have been achieved in recent years.

After the verification of the De Broglie hypothesis, the next important step towards a practical electron microscope has been the the development of the **magnetic lens** (H. Busch, 1926, fig. 4), followed by the demonstration of focussing by electric fields. These discoveries led to rapid progress, so much so that the first electron microscope was constructed by M. Knoll and E. Ruska in 1931. This first instrument worked in *transmission*, like the modern-day Transmission Electron Microscope or TEM, and had a resolution of several nm. The TEM was later developed as a commercial device, and now reaches routinely resolutions of the order of 1-2 Å, with sub-Å resolutions having been demonstrated in specialised instruments.

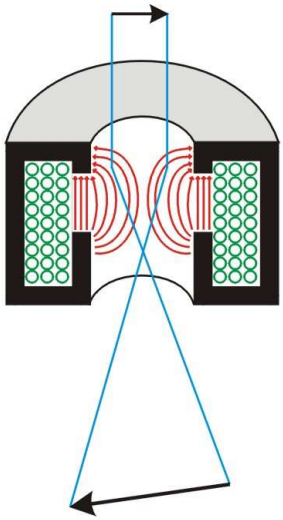

Figure 4: Schematic representation of a TEM magnetic lens. The trajectory of the electrons in this lens is quite complex, so that the image is rotated as well as magnified.

A different type of electron microscope, known as Scanning Electron Microscope or SEM, was built in 1938 by M. von Ardenne, following a suggestion by Knoll. In the SEM, the electron beam is electrically "scanned" across the surface of the sample producing a small spot, and a response (backscattered electrons, Auger electrons, X-rays etc.) is measured. An image of the sample is then formed on the screen using the measured variable. The importance of both TEM and SEM for materials science cannot be overstated. However the TEM has been far more important to solve problems in structural condensed matter physics, and we will therefore limit our brief

discussion to the Transmission Electron Microscope.

Table 1: Electron wavelengths and energies and the corresponding TEM techniques. For non-relativistic electrons, $\lambda = h(2meV)^{-1} = 12.26V^{-1}$ Å. HEED wavelengths are corrected for relativistic effects ($\sim 5\%$ at 10^5 V.)

V(volts)	λ (Å)	v/c	name
10	3.9	0.006	LEED
10^2	1.2	0.02	LEED
10^3	0.39	0.06	MEED
10^4	0.12	0.19	MEED
10^5	0.037	0.54	HEED
10^6	0.009	0.94	HEED

6.2 The TEM: working principle and operating parameters

Very schematically, a TEM can be described as follows (fig. 5):

- A quasi-monochromatic beam of electron is produced and accelerated to a working voltage by an **electron gun**. The electrons are emitted by either a thermoionic filament or, in modern instrument, by a **field-emission source**, which is more monochromatic and has much higher brightness. The relation between accelerating voltage and wavelength is:

$$\lambda = \frac{h}{\sqrt{2meV}} = \frac{12.26}{\sqrt{V}}\text{Å} \tag{26}$$

  Typical accelerating voltages and corresponding wavelengths for various applications are shown in tab. 1.

- A series of magnetic lenses, collectively known as the **condenser**, create a spot size on the sample that can be varied with the excitation current of the magnetic lenses, but can be as small as 1 μm. This spot defines the field of view of the instrument, and it is ultimately imaged on the screen, yielding magnifications in excess of 300,000. The beam divergence on the sample is of the order of 10^{-3} radians, so it can be often considered as quasi-parallel.

- The **sample stage** consists of a sample holder (the sample — either a very thin section or a series of grains from a powder sample, is usually supported by a fine carbon mesh) and a titling stage, which enables the sample to be oriented so that different "zones" are brought into Bragg condition (see below). Since the sample itself is very thin (usually < 1000Å), a significant fraction of the electrons are either transmitted or undergo Bragg scattering — in both cases emerging as quasi-parallel rays. Because of the very short wavelength and the decaying atomic scattering factor, electron scattering is strongly peaked in the forward

direction and the whole diffraction pattern is concentrated within 1-2 deg for 100 KeV electrons.

- Immediately below the sample the **objective lens** brings parallel rays emerging from the sample into focus on the so-called **back focal plane**. In other words, both the direct beam and each of the Bragg reflections will be brought into a distinct spot on the back focal plane, forming a **diffraction pattern**. Here, a series of diaphragms (**diffraction apertures**) can be inserted to select the direct beam and/or one or one or more of the Bragg spots. The microscope is said to operate in (**bright-field mode**) if the transmitted beam is allowed to propagate beyond the diffraction apertures.

- Below the back focal plane, a series of lenses and apertures known collectively as the **projector** magnify and focus the electrons the so that the image of the spot fills the viewing screen.

- The image is formed on an **electron detector**, which was a simple phosphor screen in the early models, and has now evolved in a much more sophisticated and sensitive device such as a CCD or a solid-state detector.

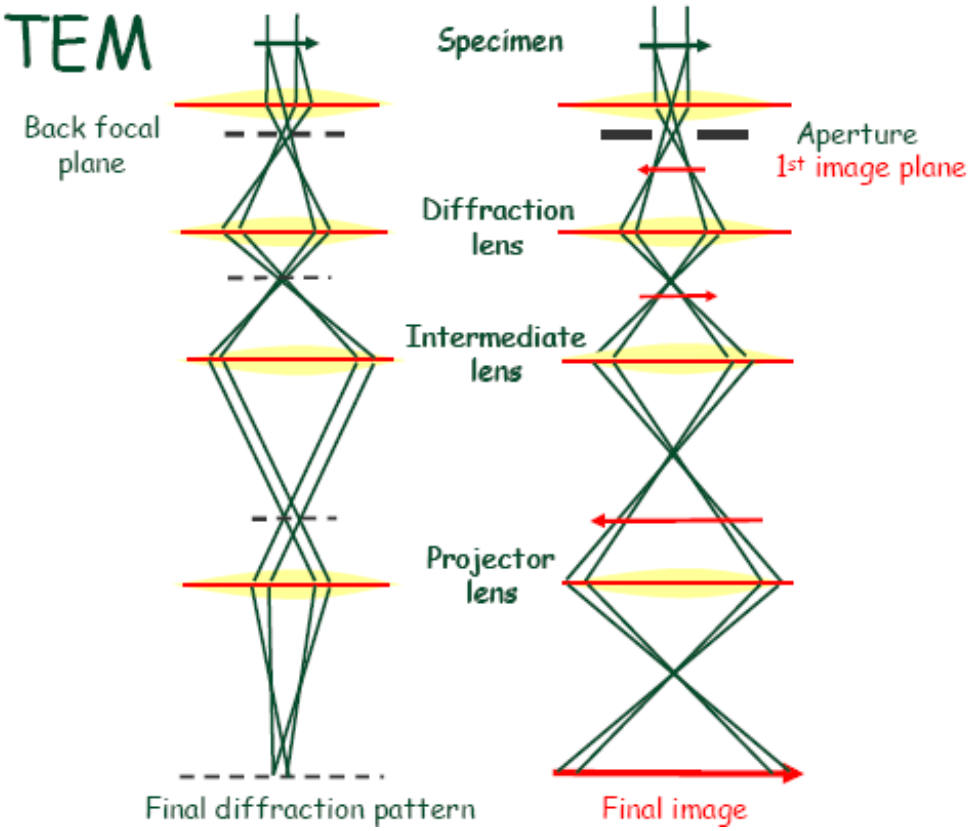

Figure 5: Schematic representation of a TEM in diffraction mode (left) and imaging mode (right).

6.2.1 Diffraction and imaging modes of operation

Broadly speaking, the TEM can be operated in two modes (see again fig. 5):

Diffraction mode: the projector brings into focus onto the detector a **magnified image of the back focal plane**, so that the diffraction pattern from the sample appears on the screen.

Imaging mode: here, the projector brings into focus onto the detector a **magnified image of the sample spot**, so that an "image" of the sample is created. Unlike conventional microscopy, where the contrast is primarily due to differential absorption of light, **for crystalline sample, contrast in TEM is primarily due to a modulation of the strength of diffraction from different parts of the sample**. The role of the diffraction apertures should become clear at this point: by propagating electrons that have undergone different Bragg reflections, one may obtain different types of contrasts. Thiks is particularly important in the study of dislocations and stacking faults (see below).

6.3 Electron diffraction: basic principles

The kinematic of electron diffraction is governed by the fact that, in a typical TEM, **electron wavelengths are much shorted than the accessible d-spacings** — in other words, $|\mathbf{k}_i| = |\mathbf{k}_f| \gg |\mathbf{q}|$. In addition, the thickness of the sample is much smaller than the spot size, so that (by finite-size effects) the Bragg spots will be elongated in the direction of $\mathbf{k}_i$. The resulting Ewald construction is shown in fig. 7. From this, it is clear that **a sizeable portion of a RL plane can be brought into (approximate) Bragg scattering condition by setting $\mathbf{k}_i$ to be perpendicular to this plane**. An estimation of the scattered intensity for each Bragg spot, using the kinematic approximation, is provided in Appendix II. The plane in question **always contains the origin of the** RL, and is known as **zeroth-order Laue zone** $[xyz]$, where $[xyz]$ is the real-space direction *orthogonal* to it. .

When operating in diffraction mode, a TEM generates a fairly undistorted picture of a slice of reciprocal space corresponding to a zeroth-order zone (see fig. 6). If the electron energy is not very high, peaks from the first-order zone may become visible near the edge of the diffraction pattern.
Example: in a monoclinic crystal, the electron beam is directed along the $[110]$ direction in *real space*. The corresponding zone will contain the origin of the RL and the two RL vectors $(1\bar{1}0)$ and (001).

Because of the large cross section for electron scattering, **dynamical diffraction is always required for quantitative calculation of electron scattering intensities**. This means that structural solution from electron diffraction is a highly specialised field of electron microscopy.

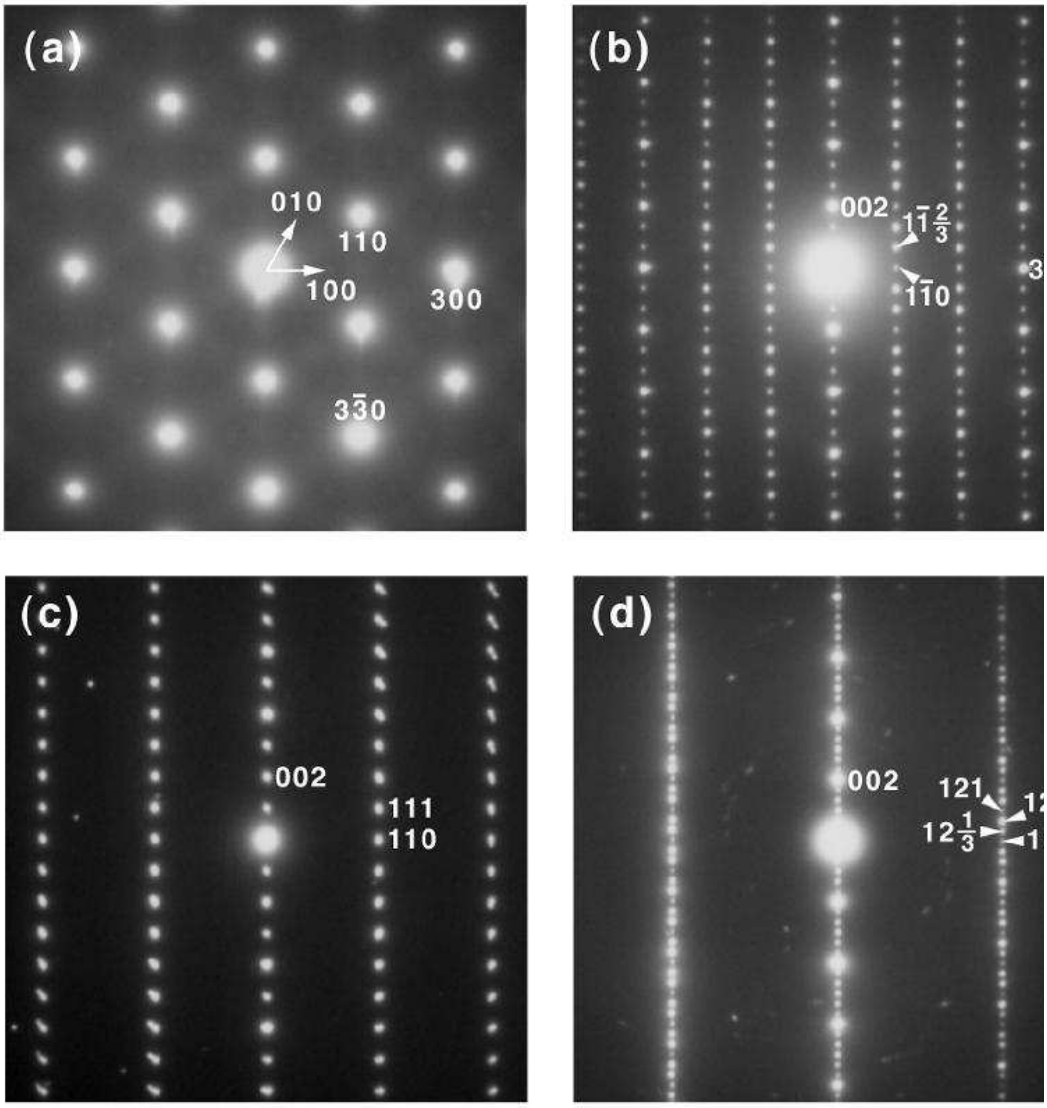

Figure 6: Sets of electron diffraction patterns of the multiferroic material YMn0.75Ti0.25O3 showing the (a) [001], (b) [110], (c) [110], and (d) [540] zone-axis. From T. Asaka, *et. al* Physical Review B **71**, 014114 (2005)

6.4 TEM imaging: basic principles

When operating in imaging mode, the projector lenses of the microscope create onto the detector an image of the *sample*. If a wide open diffraction aperture is employed, the transmitted beam

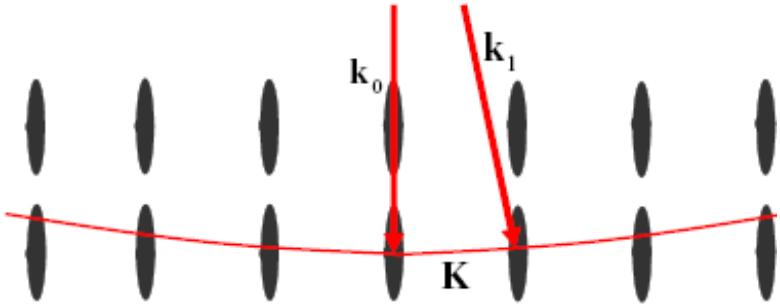

Figure 7: Ewald construction for electron diffraction.

and all the diffracted beam coming from one **specific point in the sample** are made to interfere at one **specific pixel on the detector**, and the contrast on that pixels results from the interference of these rays. By inserting appropriate diffraction apertures, one can select the transmitted beam alone and/or one or more diffracted beams. The simplest situation is that of dark-field imaging with a single reflection, since only one diffracted beam needs to be considered. Even this apparently simple scenario is rather complex to assess quantitatively:

- The "circle of confusion" of the imaging process is far from the diffraction limit, and is always dominated by the aberration of the optics. For a typical TEM, this is of the order of 1-2 Å.
- In the direction of the electron beam, the depth of field of the optics is generally sufficient to keep the whole thickness of the sample close to focussing conditions, although fine-tuning of the focus can have a dramatic effect on the contrast.
- To assess the contrast in the first approximation, therefore, one has to consider interference between the scattered beams from a **column of atoms**, contained in a cylinder defined by the circle of confusion of the optics and the thickness of the sample.

In the case of a perfect lattice, the imaging contrast has the periodicity of the lattice, and this can be easily distinguished at sufficient resolution.

Fig. 8 shows a typical example — a high-resolution lattice image of Si_3N_4. A clearly distinguishable grain boundary runs irregularly from the bottom left to the middle right of the image. The two grains have different orientations, and show different periodicity. In some images, one would be tempted to identify the repeated pattern with the content of the unit cell, as if one was looking at individual atoms, but this is never the case: a complex calculation involving dynamical diffraction end the exact focus condition is *always* require for realistic lattice image simulations.

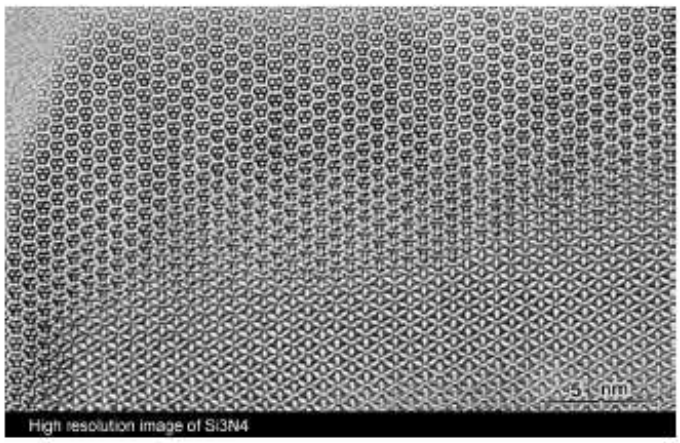

Figure 8: High-resolution image of a grain boundary in Si_3N_4.

6.4.1 TEM imaging of dislocations and stacking faults

One of the most successful applications of the TEM has been the imaging and identification of lattice defects — particularly dislocations and stacking faults. As we have seen, a dislocation or stacking fault is characterised by the fact that a portion of the crystal, either around the dislocation line or across the stacking fault, is **displaced** with respect to the rest of the crystal by a vector $\mathbf{b}$, which is known as the **Burgers vector** in the case of dislocations and the **slip vector** in the case of stacking faults. The structure factor F_f of the "faulted" region will be therefore related to that of the unfaulted region by:

$$F_f(\mathbf{q}) = F(\mathbf{q})e^{-i\mathbf{q}\cdot\mathbf{b}} \tag{27}$$

We remind that here the scattering vector $\mathbf{q}$ is **selected using the diffraction apertures**. The intensity scattered from a column (corresponding to the contrast of a pixel) can then be written as

$$I/I_0 \propto |F|^2 \left| \sum_{N=0}^{N_1} e^{-iN\mathbf{q}\cdot\mathbf{a}_z} + \sum_{N=1}^{N_2} e^{-iN\mathbf{q}\cdot(\mathbf{a}_z+\mathbf{b})} + \sum_{N=2}^{N_z} e^{-iN\mathbf{q}\cdot\mathbf{a}_z} \right|^2 \tag{28}$$

were we have assumed that the faulted region is delimited by N_1 and N_2 along the column. We could elaborate further on eq. 28, but here it will suffice to say that **the fault will have maximum contrast if the vector $\mathbf{q}$ along the Burgers or slip vector** $\mathbf{b}$, and will be **invisible if $\mathbf{q} \perp \mathbf{b}$**. By taking a series of dark-field lattice images using different Bragg reflections, it is therefore possible to identify both the **direction** of the dislocation line or fault plane (which is simply the direction of the contrast in the lattice image) and the **Burgers or slip vector**, which

are perpendicular to the Bragg reflections for which the defects become invisible (see fig. 9).

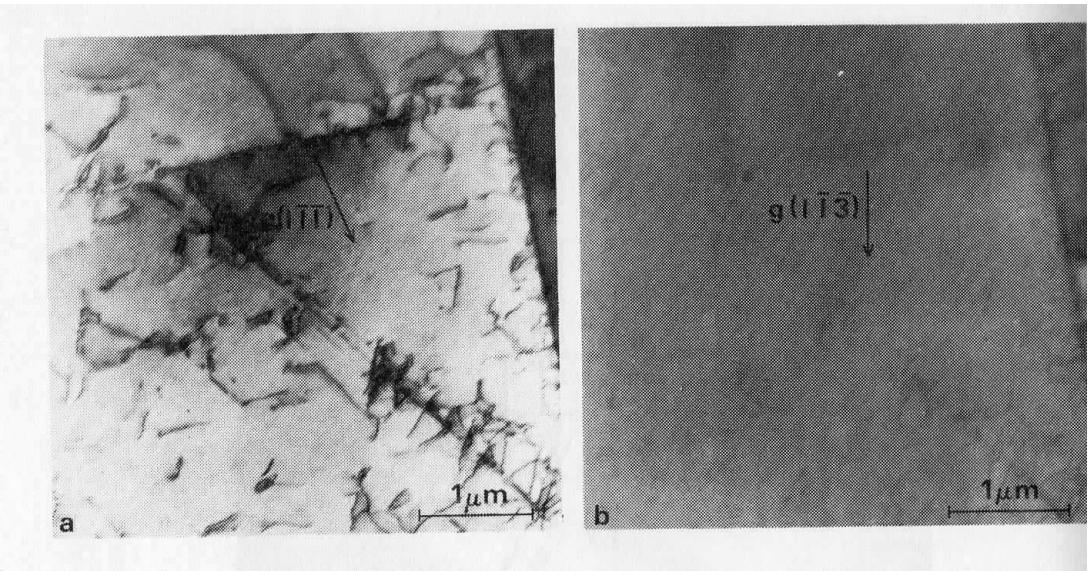

Figure 9: Reproduced from [1], fig 4.16. Images of dislocations in stainless steel. On each picture, the (hkl) of the reflection employed to create the image is marked with an arrow. **Left**: Image taken with a $(1\bar{1}1)$ reflection: many dislocations are in contrast. **Right**: Image taken with a $(1\bar{1}\bar{3})$: most dislocations are out of contrast. This analysis indicates that most dislocations have $(1\bar{1}1)$ Burgers vector.

7 Bibliography

P.J. Grundy & G.A. Jones [1] A handy booklet on electron microscopy, a bit old but still useful.

S.J.L. Billinge & M.F. Thorpe [2] A good collection of articles on diffuse scattering and scattering from disordered materials.

References

[1] P.J. Grundy and G.A. Jones T. Hahn, ed., *Electron Microscopy in the Study of Materials*, (Edward Arnold Ltd. London: UK, 1976).

[2] S.J.L. Billinge and M.F. Thorpe eds., "Local structure from diffraction", Kluwer Academic Publishers New York, Boston, Dordrecht, London, Moscow, 2002.

8 Appendix I: the pair distribution function analysis

Let us continue on from eq. 25 and introduce a continuous function $\rho(r_{ij})$ (of dimensions $[m^{-3}]$) representing the "local number densities" of atoms at a distance r_{ij} around a given atom (excluding itself). The function $\rho(r_{ij})$, known as the **pair distribution function** will be zero at short distances and will have a sharp peak corresponding to the first coordination shell, with further oscillations corresponding to more distant correlations At long distances, $\rho(r_{ij})$ will converge to the *average density* ρ_a. For a typical glass, this occurs at distance of the order of 10-20 Å, whereas for a crystal the oscillations persist to very long distances. Observing that(we drop the subscripts ij at this point)

$$n(r) = 4\pi r^2 \rho(r) dr \tag{29}$$

we replace the sum with an integral in eq. 25 and write:

$$\frac{d\sigma}{d\Omega} = N r_0^2 \mathcal{P}(\gamma) |f(\mathbf{q})|^2 \left[1 + \int_0^\infty dr 4\pi r^2 \rho(r) \frac{\sin qr}{qr} \right] \tag{30}$$

If we now write $\rho(r) = \rho_a + \Delta\rho(r)$, where $\Delta\rho(r)$ represents the *deviation* from the average density, we can show that the term containing ρ_a fluctuates rapidly (except at very low q, where data are usually not measured since they merge with the transmitted beam), and averages out between different domains of scattering. We thus obtain the final form:

$$\frac{d\sigma}{d\Omega} = N r_0^2 \mathcal{P}(\gamma) |f(\mathbf{q})|^2 \left[1 + \int_0^\infty dr 4\pi r^2 \Delta\rho(r) \frac{\sin qr}{qr} \right] \tag{31}$$

Let us now introduce the function

$$S(q) = \left(N r_0^2 \mathcal{P}(\gamma) |f(\mathbf{q})|^2 \right)^{-1} \frac{d\sigma}{d\Omega} \tag{32}$$

which can be directly extracted from a scattering experiment, after appropriate normalisation and correction of the data. By using the properties of the Fourier transform we find:

$$\rho(r) = \rho_a + \frac{1}{2\pi^2 r} \int_0^\infty dq \left[S(q) - 1 \right] q \sin qr \tag{33}$$

Clearly, it is impossible to measure $S(q)$ up to $q = \infty$, so the Fourier transform procedure as applied to "real" data will introduce **truncation errors**, which can be mitigated by applying

various procedures.

The Pair Distribution Function (or PDF) analysis method is widely used not only for liquid and amorphous substances, but to disordered (and sometimes rather well ordered) crystalline materials, where it claims to provided an unbiassed determination of the "true" bond lengths. When PDF analysis is applied to crystals, both Bragg and diffuse scattering are included yielding a picture of the **local structure** (as opposed to the **average structure** from Bragg scattering).

9 Appendix II: electron scattering from a thin section of sample

In this section, we give a quantitative calculation for the scattered intensity in the kinematic approximation. To be realistic, this calculation can only be applied to a very thin section of the sample, since, as we already mentioned, the elastic scattering cross section of electrons is so large that dynamic effects are dominant. In this scenario, the electron beam illuminates a region of the sample of, say, 1-2 μm in size, and are partly transmitted, partly scattered through a section a a few tens of Å. We also recall that electron scattering is strongly peaked in the forward direction and is concentrated within 1-2 deg for 100 KeV electrons. The Ewald construction appropriate for this problem is shown in fig. 7. When the incident beam is along a **real** lattice vector, several Bragg peaks of the "zeroeth-order zone" (i.e., the RL plane perpendicular to that vector and containing the origin) will be close to scattering conditions, so that a portion of the diffraction pattern for that plane will appear on the screen. Bragg peaks that are progressively more distant from the origin will be cut by the Ewald sphere "above" the ideal Bragg position. Here, we want to calculate the integrated intensity, i.e., the number of electrons collected by the film or CCD, of each of these reflections in the kinematic approximation.

Let us define the z axis in the direction of the beam, x and y being the lateral coordinates. In analogy to what we have done before, we will consider the lateral extent of the sample to be infinite, so that the cross section will contain a 2-dimensional delta function. By contrast, we will consider explicitly the finite size of the sample along z. We therefore write

$$\begin{aligned} \frac{d\sigma}{d\Omega} &= \frac{(2\pi)^2 N_x N_y}{a_x a_y}\delta(q_x)\delta(q_y)\frac{\sin^2(\frac{1}{2}N_z q_z a_z)}{\sin^2(\frac{1}{2}q_z a_z)}|F|^2 \\ &\simeq \frac{(4\pi)^2 N_x N_y}{v_0 a_z}\delta(q_x)\delta(q_y)\frac{\sin^2(\frac{1}{2}N_z q_z a_z)}{q_z^2}|F|^2 \end{aligned} \tag{34}$$

Where F is the structure factor and has the dimension of a *length*. In the geometry we are considering (fig. 7)

$$d\Omega \simeq \frac{dq_x dq_y}{k_i^2} = \frac{\lambda^2}{4\pi^2} dq_x dq_y \tag{35}$$

We can therefore integrate in $d\Omega$

$$\sigma = \frac{4N_x N_y \lambda^2}{v_0 a_z} \frac{\sin^2(\frac{1}{2}N_z q_z a_z)}{q_z^2} |F|^2 \tag{36}$$

Here, $v_0 = a_x a_y a_z$ is the unit cell volume. Now, let multiply by the incident flux, which we will write as $\Phi_0 = I_0/(N_x N_y a_x a_y)$, where I_0 is the number of incident electrons per second. This is appropriate, since here the lateral dimension of the sample (i.e., $N_x N_y$) is defined by the spot size. We thus obtain the **scattered intensity** (again, in electrons per second) in a given reflection.

$$\frac{I_h kl}{I_0} = \left| \frac{2\lambda F_{hkl}}{v_0} \right|^2 \frac{\sin^2(\frac{1}{2}q_z t)}{q_z^2} \tag{37}$$

Where we have introduced $t = N_z a_z$ — the thickness of the sample. The quantity

$$\xi_g = \frac{v_0}{2\lambda F_{hkl}} \tag{38}$$

has the dimensions of a *length*, and is known as the **extinction distance**. As we can see, the intensity has a central maximum and a series of subsidiary maxima. The height and width (distance between the two nearest minima) of the central maximum are:

$$\begin{aligned} H &= \left(\frac{t}{\xi_g}\right)^2 \\ W &= \frac{4\pi}{t} \end{aligned} \tag{39}$$

One can see that when the thickness t is equal to ξ_g, $H = 1$ and the scattered intensity is equal to the incident intensity (**total reflection**). This is a clear signal that the kinematic approximation is no longer applicable. Typical extinction distances are of the order of 10 nm. It is a matter of simple geometry to show that the principal and subsidiary maxima can be intersected by the Ewald sphere, giving rise to scattering corresponding to a given Bragg peak in the diffraction pattern.